

Study of Electron-Beam Propagation through Preionized Dense Foam Plasmas

R. Jung,¹ J. Osterholz,¹ K. Löwenbrück,¹ S. Kiselev,¹ G. Pretzler,¹ A. Pukhov,¹ O. Willi,¹ S. Kar,² M. Borghesi,² W. Nazarov,³ S. Karsch,⁴ R. Clarke,⁴ and D. Neely⁴

¹Heinrich-Heine-Universität Düsseldorf, D-40225 Düsseldorf, Germany

²Queen's University of Belfast, Belfast BT7 1NN, United Kingdom

³University of Dundee, Dundee DD1 4HN, United Kingdom

⁴Rutherford Appleton Laboratory, Chilton, Didcot, Oxon OX11 0QX, United Kingdom

(Received 9 September 2004; published 16 May 2005)

The transport of an intense electron-beam produced by the Vulcan petawatt laser through dense plasmas has been studied by imaging with high resolution the optical emission due to electron transit through the rear side of coated foam targets. It is observed that the MeV-electron beam undergoes strong filamentation and the filaments organize themselves in a ringlike structure. This behavior has been modeled using particle-in-cell simulations of the laser-plasma interaction as well as of the transport of the electron beam through the preionized plasma. In the simulations the filamentary structures are reproduced and attributed to the Weibel instability.

DOI: 10.1103/PhysRevLett.94.195001

PACS numbers: 52.38.Kd, 41.75.Jv, 52.40.Mj, 52.57.Kk

The understanding of the transport of high energy electrons through matter is of fundamental importance, for example, for the fast ignitor (FI) concept relevant to laser fusion and astrophysical applications. In the FI concept, ignition of a precompressed pellet containing the fusion fuel is initiated by laser produced electrons with energies in the MeV range [1]. The main advantages of fast ignition with respect to direct or indirect drive are significantly relaxed symmetry requirements on the implosion and the possibility of achieving higher gain [1–4]. It is crucial for this scheme that the energy of the ignitor laser is efficiently converted into an intense electron beam that can propagate through the high density overdense plasma and initiate the thermonuclear burn in the precompressed core [5]. Several processes are known that contribute to the acceleration of electrons in plasmas such as resonance absorption, $\vec{j} \times \vec{B}$ heating, and direct laser acceleration [6–8]. Measurements show that up to 50% of the laser energy can be transferred into kinetic energy of fast electrons [9].

The transport of the electrons to the precompressed core involves currents of the order of 100–1000 MA through regions of overdense plasma. These currents exceed the critical Alfvén limit given by $J_A = 17.1\beta\gamma$ kA, where $\beta = v/c$ and γ is the relativistic Lorentz factor [10]. This is possible only if return currents which are formed by the thermal background electrons of the plasma play a significant role in neutralization.

Under these conditions, i.e., in the presence of a large flow of fast electrons and a counterstreaming flow of cold electrons, kinetic instabilities like the Weibel instability [11] can grow. Two-dimensional and three-dimensional particle-in-cell (PIC) simulations have clearly predicted that the transport of the relativistic electron-beam is not homogenous, but filamentary structures will occur. Magnetic fields up to 100 MG are predicted to surround the filaments [12,13]. The arrangement of the filaments

propagating through the region of overdense plasma is of great interest because it determines the amount of energy that can be deposited in the fuel. Processes such as collective stopping of the hot electrons, coalescence of the current filaments, and energy dissipation due to heating of the surrounding plasma can all play a significant role [14,15]. Therefore the understanding of the propagation mechanisms of the relativistic electrons through dense plasmas is essential for the success of the FI scheme.

A number of experiments investigating the propagation and filamentation of laser produced relativistic electron beams have been performed using metal and plastic foils or glass slabs [16–22]. Preheated low density foam targets offer a different approach to study electron-beam transport through dense plasmas over long distances. In terms of target resistivity this approach is possibly more relevant to the FI scheme. Being much less collisional than solid target plasmas, they are also ideal testbeds for PIC simulations.

Here we report on experimental data and simulations using preionized CH-foam targets. The electrons exiting the rear surface of the target were diagnosed by imaging the associated optical emission with high spatial resolution. The images suggest filamentation of the electron beam with a transverse scale length of a few microns. Around the center the filaments organize themselves into a ringlike structure, surrounded by a cloud of several smaller filaments. A detailed analysis has been performed using 3D PIC simulations to calculate the electron energy distribution. In addition, the propagation of an electron beam was simulated using the calculated electron distribution. The numerical results clearly show filamentary structures in qualitative agreement with the experimental data.

The experimental measurements were carried out at the Vulcan Petawatt Laser Facility at the Rutherford Appleton Laboratory. A 350 J laser pulse with a wavelength of $\lambda_0 = 1053$ nm and 750 fs in duration was focused with an $f/3.2$

parabola onto low density foam targets with various thicknesses at an angle of incidence of 45° . This gave a reproducible focal spot of $6 \mu\text{m}$ in diameter containing about 75% of the laser energy. Figure 1 schematically shows the geometry of the experimental setup. The rear side of the target was simultaneously imaged onto two cameras loaded with Ilford HP5 film using an $f/2$ lens system with a focal length of $f = 100 \text{ mm}$ and nonpolarizing beam splitters. The magnification was $40\times$. The resolution of the imaging system was experimentally confirmed to be better than $2 \mu\text{m}$. In order to achieve high spatial resolution, the spectral window of one of the two cameras used was limited to a bandwidth of $\Delta\lambda = 10 \text{ nm}$ around the central wavelength of the second harmonic of the laser at 527 nm by using an interference filter. The second camera integrated over the visible spectral range. Spectra of the light emitted were recorded with an optical spectrometer operating at the central wavelength of 527 nm and detected with a 16-bit CCD camera. The stray light of the petawatt infrared laser beam was blocked using KG5 filters. The spectral sensitivity range of the imaging system was 400 to 700 nm. The energies of the electrons emitted at the rear side of the target were measured with a permanent-magnet electron spectrometer [23] along the axis of the laser beam. The distance from the target to the 5 mm diameter collimator was 3.7 m, resulting in a solid angle of $1.4 \times 10^{-6} \text{ sr}$. The electron spectra were recorded on Fujifilm image plates.

Coated targets with a cell size of $1 \mu\text{m}$ and densities of 100 and 200 mg/cm^3 were used. The thicknesses were 250, 500, and $750 \mu\text{m}$. The front side of the foams was overcoated with a 75 nm gold layer. This was done in order to generate a radiation wave produced by the leading edge of the laser pulse for preionization of the foam [24,25]. With a 75 nm gold layer a radiation wave with a temperature of about 150 eV is expected producing a plasma with an electron density between 15 and 30 times critical density depending on the target density used. The rear side of the targets was overcoated with 200 nm of

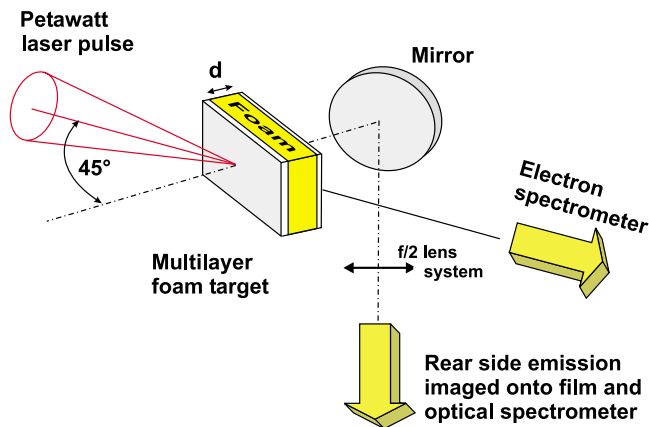


FIG. 1 (color). Setup and target layout.

aluminum in order to obtain a sharp density gradient important for the optical transition radiation technique [26]. The direct propagation of the second harmonic of the laser beam was effectively prevented by the overdense target plasma and the aluminum coating at the rear side of the target.

Figure 2 shows typical electron spectra obtained for different target conditions. As can be seen the different density targets gave similar results. A two temperature Boltzmann distribution was obtained with a “hot” temperature of around $T_h \approx 9 \text{ MeV}$ and a “cold” temperature of $T_c \approx 3 \text{ MeV}$.

The optical spectra and the comparison of the images with and without the bandpass filter showed that the emission collected by the optics peaked significantly around the second harmonic of the laser frequency. Following Ref. [27] such emission can be explained as coherent transition radiation due to hot electrons transiting through the rear target-vacuum interface, although some contribution from synchrotron emission cannot be excluded *a priori*. The bandwidth of the peak is $\Delta\lambda_p = 4 \text{ nm}$ (FWHM) (in comparison the laser spectral bandwidth is $\Delta\lambda_L = 2.2 \text{ nm}$). The coherence of the emission is also confirmed as in some of the images an interference pattern is observed. This indicates that the electrons are accelerated in bunches either twice or once per optical cycle $\tau_0 = 2\pi/\omega_0$ of the petawatt laser pulse, as previously observed by other groups [17,21,27]. In those investigations electron bunching has been attributed to either the laser ponderomotive force or resonance absorption. While the oscillating component of the ponderomotive force will accelerate bunches of electrons twice every laser cycle, this would happen only once per cycle in the resonance absorption case.

We calculated the effective temperatures for the conditions defined by our laser parameters as determined by these two mechanisms. According to the model given by

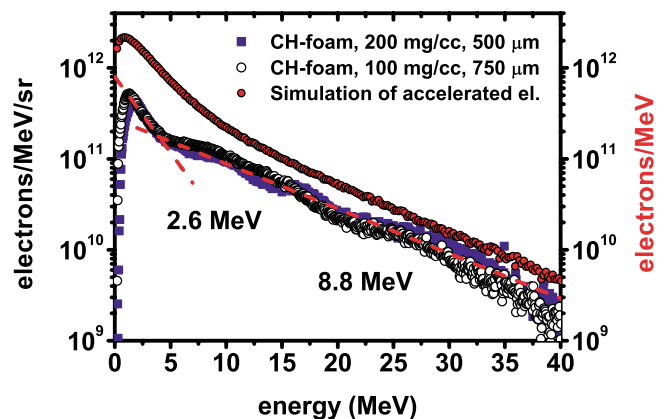


FIG. 2 (color). Electron spectra measured for different foam target conditions and spectrum obtained from the simulation for similar target and laser conditions (total number per MeV).

Wilks *et al.* [8] the laser ponderomotive force will lead to an effective temperature of

$$T_{\text{pm}} = 0.511[(1 + I_{18}\lambda_L^2/1.37)^{1/2} - 1] \text{ MeV}, \quad (1)$$

while resonance absorption will contribute to a Boltzmann distribution with a temperature given by [6]

$$T_{\text{res}} = 0.1(I_{17}\lambda_L^2)^{1/3} \text{ MeV} \quad (2)$$

with λ_L as the wavelength of the accelerating laser pulse (in μm , I_{17} and I_{18} denote the intensity in terms of 10^{17} and 10^{18} W/cm^2 , respectively). Equation (2) is valid only for p -polarized radiation (as was the case in the experiment). It is well-known that electrons accelerated by resonance absorption of the laser pulse will be directed perpendicular to the target surface (due to the direction of the density gradient), while the laser ponderomotive force at high intensities accelerates electrons along the laser propagation axis [6,28–30]. In our experiment the optical emission at the target rear was observed in the direction of the laser axis. On this basis it seems reasonable to assume that the emission observed was due to ponderomotively accelerated electrons bunched at $2\omega_0$. We compared the temperatures measured with those predicted according to Eqs. (1) and (2): The intensity on the different targets was between 3.5 and $5 \times 10^{20} \text{ W/cm}^2$, which leads to T_h between 7.5 and 9.3 MeV and $T_c \approx 2 \text{ MeV}$. The values derived from the measured spectra for the two temperatures are close to the estimated ones.

A typical optical image taken on a foam target is shown in Fig. 3. The thickness was $250 \mu\text{m}$; the density of the foam was 100 mg/cm^3 . The data were processed by overlying the two images obtained on the same shot.

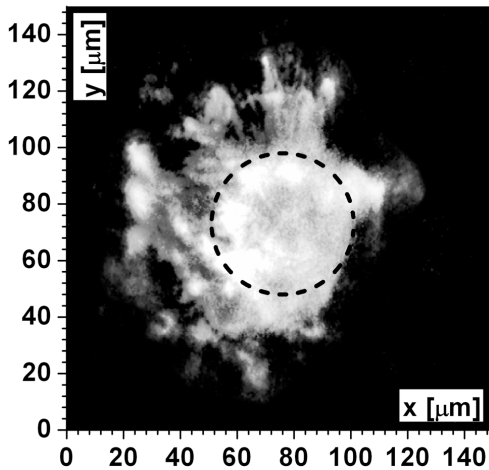


FIG. 3. Optical emission data obtained using a $250 \mu\text{m}$ foam target. The image shows the reprocessed data obtained from both cameras with different gray filters by overlying in order to show the substructure of the inner circle as well as the filaments in the outer region. The positions of the inner filaments are indicated with a circle with $50 \mu\text{m}$ in diameter, whereas the spot including the filaments in the outer region has a diameter up to $100 \mu\text{m}$.

Since in the setup the optical axis of the diagnostics was perpendicular to the target rear side (see Fig. 1), the angle between the cone of exiting beamlets and the target rear surface caused an elongation in width of the images. To correct this, the horizontal direction has been rescaled. In Fig. 3 filaments with spot sizes of $\sim 10 \mu\text{m}$ in diameter (FWHM) are observed that are clearly organized in a ringlike structure. The diameter of the ring indicated in Fig. 3 is about $50 \mu\text{m}$. The filaments are surrounded by a cloud of several smaller filaments, where the size of smallest observable filaments is about $\sim 2 \mu\text{m}$. The analysis of the divergence of the filaments with increasing target thickness reveals a divergence angle of $\sim 10^\circ$ for the ring and $\sim 20^\circ$ for the cloud of outer filaments.

Simulations were carried out for the experimental parameters with the 3D PIC code Virtual Laser Plasma Laboratory [31]. In the first step we have used a laser pulse with the Gaussian profile $a = a_0 \exp[-(t/T)^2 - (r/R)^2] \cos[\omega_0(t - cz)]$, where $a_0 = 15$, $T = 314\omega_0^{-1}$, and $R = 63c/\omega_0$. The laser was normally incident onto a plasma layer with a linear density ramp reaching the maximum $N_{\text{max}} = 20N_c$ over the distance $L = 300c/\omega_0$, where $N_c = \omega_0^2 m/4\pi e^2$ is the critical density (for a laser wavelength of $1.053 \mu\text{m}$, $N_c = 1.1 \times 10^{21} \text{ cm}^{-3}$). The linear density ramp was used to mimic the preplasma at the target surface. The spectrum of the total accelerated electrons is shown in Fig. 2. The calculated spectrum consists of two Boltzmann-like energy distributions with $T_{\text{eff}} \approx 8$ and 3.5 MeV .

In the second step, the electron-beam was injected into a plasma with $N_e = 30N_c$ and its propagation was studied. The simulations were carried out for the higher density target as the measured electron spectra were similar for the 100 and 200 mg target. The transverse electron-beam temperature was set to zero to keep the beam within the simulation box. Initially, the electron beam had a smooth Gaussian transverse density profile with radius $R_b = 10 \mu\text{m}$ and a peak density of $N_b = 0.1N_c$. This beam transports the power $P_b = \gamma N_b m c^3 \pi R_b^2 \approx 14 \text{ TW}$ and the current $J = N_b e c \pi R_b^2 \approx 7J_A \approx 1.8 \text{ MA}$. The electron-beam current is significantly above the Alfvén limit, and the beam quickly begins to filament. Figure 4 shows transverse cuts of the electron density and the x component of the quasistatic magnetic field after the beam has propagated 10 , 20 , and $100 \mu\text{m}$ through the foam plasma. The onset of the filamentation is observed at a radius $\sim R_b$ after the beam has propagated about $10 \mu\text{m}$ [Figs. 4(a) and 4(b)]. This can be explained with small perturbations in the magnetic repulsion of the counterstreaming beams. After a propagation distance of $20 \mu\text{m}$, strong magnetic fields are observed at a radius $r \approx 7 \mu\text{m}$ and cause the inner part of the beam to filament [Figs. 4(c) and 4(d)]. This leads to the occurrence of the inner current filaments observed. Then some of the filaments begin to merge while the ringlike geometry survives. After a propa-

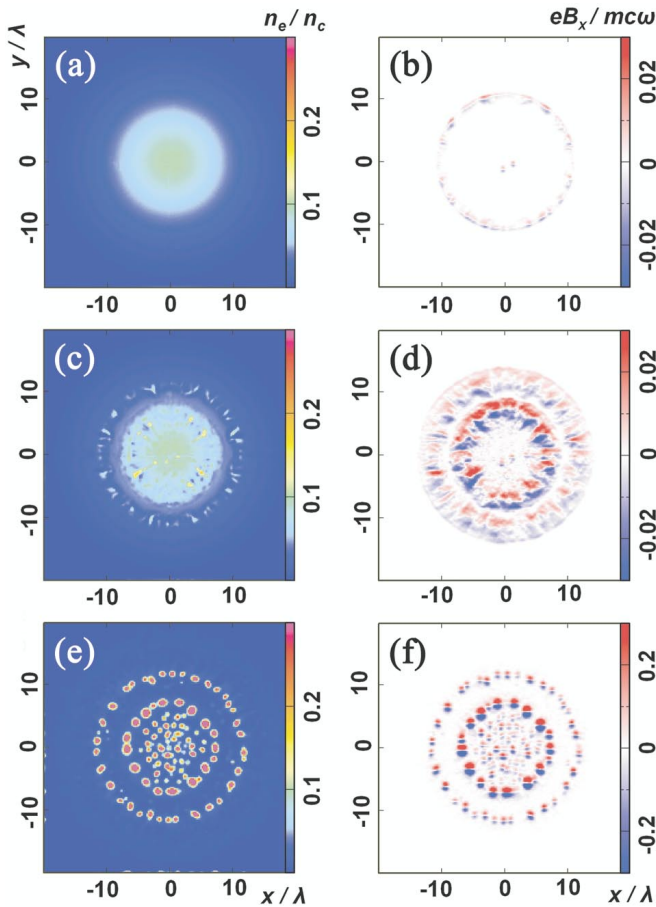


FIG. 4 (color). Simulation of electron density of hot electrons after 10, 20, and 100 μm propagation [(a),(c),(e)] and x component of the magnetic field surrounding the filaments [(b),(d),(f)].

gation of 100 μm the formation of ring structures in the filamentation pattern is observed [Figs. 4(e) and 4(f)]. Note that a similar structure has been observed in the experiment.

According to analytical predictions, filamentation due to the Weibel instability is expected to grow on a time scale of the plasma frequency of the relativistic electron beam, ω_{be} , and the growth rate of the instability, $\gamma_{\text{inst}} \approx \omega_{\text{be}} [N_b / (\gamma N_e)] v / c$, scales with the beam contrast N_b / N_e , where N_e is the density of the surrounding plasma [14,32]. Using $N_b = 0.1 N_e$, $N_e = 30 N_e$, and $v \sim c$, and estimating the growth rate of the Weibel instability, one obtains $\gamma_{\text{inst}}^{-1} \sim 130$ fs. This corresponds to a beam propagation distance of about 40 μm which is of the same order as that observed in the simulation. Each small filament in Fig. 4(e) carries a current smaller than the limiting Alfvén current J_A and is surrounded by a self-generated magnetic field. The B_x field reaches 30 MG [Fig. 4(f)]. Thus we assume that it is this magnetic field that leads to beam filamentation due to the Weibel instability.

To summarize, we have studied relativistic electron-beam propagation through dense plasmas using preionized CH-foam targets. High resolution images of the optical radiation emitted by MeV electrons at the rear side have been taken. The optical emission is ascribed to coherent transition radiation produced by electron bunches. It is observed that the electron beam breaks up into filaments. The role of the Weibel instability in initiating the filamentation process is inferred from 3D PIC simulations and simple analytical considerations.

We would like to acknowledge the EU Large Facility Programme under which this experimental study was funded. This work has been performed within the SFB/Transregio TR 18. In addition, the partial support by the QUB IRCEP and the excellent service of the RAL staff are acknowledged.

-
- [1] M. Tabak *et al.*, Phys. Plasmas **1**, 1626 (1994).
 - [2] R. E. Kidder, Nucl. Fusion **16**, 405 (1976).
 - [3] S. Atzeni and M. L. Ciampi, Nucl. Fusion **37**, 1665 (1997).
 - [4] R. Kodama *et al.*, Nature (London) **412**, 798 (2001).
 - [5] C. Deutsch, H. Furukawa, K. Mima, M. Murakami, and K. Nishihara, Phys. Rev. Lett. **77**, 2483 (1996).
 - [6] F. Beg, Phys. Plasmas **4**, 447 (1997).
 - [7] A. Pukhov, Phys. Plasmas **6**, 2847 (1999).
 - [8] S. C. Wilks, W. L. Kruer, M. Tabak, and A. B. Langdon, Phys. Rev. Lett. **69**, 1383 (1992).
 - [9] S. Hatchett *et al.*, Phys. Plasmas **7**, 2076 (2000).
 - [10] H. Alfvén, Phys. Rev. **55**, 425 (1939).
 - [11] E. Weibel, Phys. Rev. Lett. **2**, 83 (1959).
 - [12] T. Taguchi, T. M. Antonsen, C. S. Liu, and K. Mima, Phys. Rev. Lett. **86**, 5055 (2001).
 - [13] A. Pukhov, Rep. Prog. Phys. **66**, 47 (2003).
 - [14] M. Honda, J. Meyer-ter-Vehn, and A. Pukhov, Phys. Rev. Lett. **85**, 2128 (2000).
 - [15] Y. Sentoku *et al.*, Phys. Rev. E **65**, 046408 (2002).
 - [16] M. Tatarakis *et al.*, Phys. Rev. Lett. **81**, 999 (1998).
 - [17] J. Zheng *et al.*, Phys. Rev. Lett. **92**, 165001 (2004).
 - [18] T. Hall *et al.*, Phys. Rev. Lett. **81**, 1003 (1998).
 - [19] H. Teng *et al.*, Phys. Rev. E **67**, 026408 (2003).
 - [20] J. Fuchs *et al.*, Phys. Rev. Lett. **91**, 255002 (2003).
 - [21] J. Santos *et al.*, Phys. Rev. Lett. **89**, 025001 (2002).
 - [22] M. Borghesi *et al.*, Phys. Rev. Lett. **83**, 4309 (1999).
 - [23] P. Norreys, Phys. Plasmas **11**, 2746 (2004).
 - [24] T. Afshar-rad *et al.*, Phys. Rev. Lett. **73**, 74 (1994).
 - [25] M. Desselberger, M. W. Jones, J. Edwards, M. Dunne, and O. Willi, Phys. Rev. Lett. **74**, 2961 (1995).
 - [26] V. Ginzburg and V. Tsytovich, *Transition Radiation and Transition Scattering* (Hilger, Bristol, 1990).
 - [27] S. Baton *et al.*, Phys. Rev. Lett. **91**, 105001 (2003).
 - [28] G. Malka and J. L. Miquel, Phys. Rev. Lett. **77**, 75 (1996).
 - [29] M. Santala *et al.*, Phys. Rev. Lett. **84**, 1459 (2000).
 - [30] Z. Sheng *et al.*, Phys. Rev. Lett. **85**, 5340 (2000).
 - [31] A. Pukhov, J. Plasma Phys. **61**, 425 (1999).
 - [32] R. Evans, L. Silvia, J. Davies, and W. B. Mori, Central Laser Facility, Rutherford Appleton Laboratory Annual Report No. 2002/2003, 2003.